

Optical identification of the 3C 58 pulsar wind nebula

Yu. A. Shibano¹, N. Lundqvist², P. Lundqvist², J. Sollerman^{2,3}, and D. Zyuzin⁴

¹ Ioffe Physical Technical Institute, Politekhnicheskaya 26, St. Petersburg, 194021, Russia

² Stockholm Observatory, AlbaNova Science Center, Department of Astronomy, SE-106 91 Stockholm, Sweden

³ Dark Cosmology Center, Copenhagen, Denmark

⁴ Academical Physical Technical University, Khlopina 8, St. Petersburg, 195220, Russia

Preprint online version: August 5, 2021

ABSTRACT

Aims. 3C 58 is a Crab-like supernova remnant containing the young pulsar PSR J0295+6449, which powers a radio plerion and a compact torus-like pulsar wind nebula visible in X-rays. We have performed a deep optical imaging of the 3C 58 field with the Nordic Optical Telescope in the *B* and *V* bands to detect the optical counterpart of the pulsar and its wind nebula.

Methods. We analyzed our data together with the archival data obtained with the Chandra/ACIS and HRC in X-rays and with the Spitzer/IRAC in the mid-infrared.

Results. We detect a faint extended elliptical optical object with $B=24^m06\pm0.08$ and $V=23^m11\pm0.04$ whose peak brightness and center position are consistent at the sub-arcsecond level with the position of the pulsar. The morphology and orientation of the object are in excellent agreement with the torus region of the pulsar wind nebula, seen almost edge on in the X-rays, although its extension is only about a half of that in X-rays. This suggests that in the optical we see only the brightest central part of the torus with the pulsar. The object is also practically identical to the counterpart of the torus region recently detected in the mid-infrared. We estimate that the contribution of the pulsar to the observed optical flux is $\lesssim 10\%$. Combining the optical/mid-infrared fluxes and the X-ray power-law spectrum extracted from the spatial region constrained by the optical/infrared source extent we compile a tentative multi-wavelength spectrum of the central part of the nebula. Within the uncertainties of the interstellar extinction towards 3C 58 it is reminiscent of either the Crab or PSR B0540-69 pulsar wind nebula spectra.

Conclusions. The properties of the detected object strongly suggest it to be the optical counterpart of the 3C 58 pulsar + its wind nebula system. This makes 3C 58 the third member of such a class of the torus-like pulsar+nebula systems identified in the optical and mid-infrared.

Key words. pulsars – pulsar wind nebulae – optical identification

1. Introduction

The “Crab-like” supernova remnant (SNR) 3C 58 was first discovered in the radio (Weiler & Seielstad, 1971) and then identified in the optical by observations in $H\alpha$ (van den Bergh, 1978). Just as the Crab nebula, this SNR has a plerionic, or filled center. It shows a filamentary structure in the $H\alpha$ emission and in the radio with a flat radio spectrum of synchrotron origin. The distance, $d = 3.2$ kpc, and size, $\sim 6' \times 9'$ of 3C 58 is also similar to that of the Crab SNR. What makes SNR 3C 58 particularly interesting is its possible association (Stephenson & Green, 2002) with the historical supernova SN 1181. The deduced age of ~ 830 yr is consistent with the remnant being of roughly the same size as the Crab nebula, but this has been questioned on another grounds (see below).

It was long suspected that 3C 58 contains a pulsar in its center (Becker, Helfand & Szymkowiak, 1982), and after several years of searching in X-rays and radio, the pulsar J0205+6449 with a period of $P = 65.68$ ms was discovered with the Chandra X-ray observatory at the center of the SNR plerion (Murray et al., 2002). It was directly confirmed also in the radio (Malofeev

et al., 2001; Camilo et al., 2002; Malofeev et al., 2003). Deeper Chandra exposures revealed a Crab-like X-ray torus+jet pulsar wind nebula (PWN) in the center of the pulsar powered plerion (Slane et al., 2004).

One of the puzzles of the 3C 58 system is that, unlike for the Crab, the characteristic age of the 3C 58 pulsar, $\tau = P/2\dot{P} \approx 5400$ yr, is considerably higher than the historical age of 830 yr. This can perhaps be understood by assuming a larger initial spin period of the neutron star (NS). However, the factor of ~ 2 lower radial velocities of the optical (Fesen, 1983; Fesen et al., 2008) and radio (Bietenholz, Kassim, Weiler, 2001; Bietenholz, 2007) filaments than for the Crab, i.e., $\lesssim 900$ km s⁻¹, either would require a larger actual age of 3C 58, a weaker SN explosion, or a substantial deceleration of the remnant (Chevalier, 2004). Furthermore, the radio emission of 3C 58 is about 10 times fainter than for the Crab while its X-ray nebula is about 2000 times weaker. The latter is surprising and does not match the present spin-down power of the pulsar: the spindown luminosity of PSR J0205+6449 is $\dot{E} = 2.7 \times 10^{37}$ erg s⁻¹, and thus 5% of that of the Crab (this is actually the third

largest spin-down power for all known pulsars in the Galaxy). Deeper studies of PSR J0205+6449 and its PWN at different wavelengths may help to establish a link between the properties of this Crab-like SNR and its pulsar activity.

Multiwavelength studies of PSR J0205+6449 are still rare. Its radio luminosity is lower than for 99% of all known pulsars and actually the lowest among known young pulsars (Camilo et al., 2002). The X-ray properties of the nonthermal emission of the pulsar (spectral slope, pulse shape) are similar to those of the Crab. However, an important difference is the presence of a thermal blackbody-like component from the surface of the cooling NS with a temperature of about 10^6 K (Slane et al., 2004). Assuming an age of 830 yr, this temperature falls far below the predictions of the standard NS cooling theories and could suggest an enhanced cooling provided by the presence of exotic matter (like pion condensates) in the NS interior. The spectral index of the X-ray synchrotron emission from the torus-like PWN is compatible with that of the Crab, but the luminosity, $\sim 5.3 \times 10^{33}$ erg s $^{-1}$, is about 4000 times smaller. The size of the plerion core visible in X-rays, ≤ 0.55 pc, is only a factor of 3 smaller than that of the Crab.

There have been few studies of the 3C 58 field in the optical range, and we are not aware of any deep broadband imaging of the remnant. Such studies, carried out to reveal the continuum emission from the pulsar and the PWN and thus to constrain the properties of the multiwavelength spectral energy distribution, have been performed for the Crab and its twin in the LMC, PSR B0540-69 (e.g., Sollerman, 2003; Serafimovich et al., 2004). The latter two systems show a strong spectral break between the optical and X-rays leading to a smaller optical flux than would be expected from a simple extrapolation of the observed X-ray spectrum toward the optical range. The detection of the 3C 58 PWN in the mid-infrared (mid-IR) recently reported by Slane et al. (2008) also suggests a break between the infrared and X-rays, and perhaps multiple breaks. Optical studies are necessary to constrain the position and the number of the breaks.

Here we report on deep optical imaging of the central part of 3C 58 in the *B* and *V* bands with the Nordic Optical Telescope (NOT) on La Palma. These observations allowed us to find a likely candidate for the optical counterpart of the pulsar+PWN system. We compare our data with X-ray and mid-IR data retrieved from the Chandra and Spitzer archives. The observations and data reduction are described in Sect. 2. In Sect. 3 we present the results which are finally discussed in Sect. 4.

2. Observations and data reduction

2.1. Observations

The field of 3C 58 was observed on the night of October 22–23 2006 with the Andalucia Faint Object Spectrograph and Camera (ALFOSC¹) at the NOT during a service mode observation (program P34-026). ALFOSC was equipped with a 2048×2048 pixel CCD providing a field-of-view of $6'.5 \times 6'.5$ with the pixel size on the sky of $0''.19$. The center of 3C 58 was

imaged in the *B*- and *V*-band filters which have throughputs similar to the Bessel system. Sets of 10 min dithered exposures were obtained in each of the filters at an airmass varied in a narrow range of ~ 1.24 – 1.35 . The total exposure time was 5400 s in the *B* and 6600 s in the *V* bands. The PG0231+051 standard field (Landolt, 1992) was used for the photometric calibration, and was observed immediately after the 3C 58 field at a similar airmass. The observing conditions were rather stable with the seeing varying from $\sim 0''.6$ to $\sim 0''.9$ and with mean values of $\sim 0''.84$ and $\sim 0''.71$ in the *B* and *V* bands, respectively. Standard data reduction including bias subtraction, flat-fielding and cosmic ray rejection was performed making use of the IRAF *ccdred* package and *crrej* task. The individual images in each band were aligned and combined with the *imcombine* task.

2.2. Astrometric referencing

The astrometric referencing of the NOT images was done making use of the USNO-B1.0 catalog (Monet et al., 2002) and the IRAF tasks *ccmap*/*cctran*. We chose the resulting *B*-band image as a primary for the referencing since this image have fewer saturated stars in the field. To minimize any geometrical distortion effects we used the positions of eleven unsaturated reference stars² located within an arcminute from the center of the image. The nominal catalog position errors of the selected stars are less than $0''.1$. These stars show no considerable proper motions within a few mas yr $^{-1}$. Formal *rms* errors of the astrometric fit for the RA and Dec were $\approx 0''.059$ and $\approx 0''.062$, respectively, and maximal residuals of any reference star were $\leq 0''.1$ for both coordinates. Using a set of stars with good Point Spread Functions (PSFs) the *V* band image was aligned to the *B* band image with an accuracy of better than ≈ 0.1 pixel, or $\approx 0''.019$. Combining the errors, a conservative estimate of our 1σ astrometric referencing accuracy is $\leq 0''.1$ in both RA and Dec for both bands.

2.3. Photometric calibration

The observing night was photometric. The photometric calibration was carried out using six standard stars from the Landolt field PG0231+051 (Landolt, 1992) and the IRAF packages *daophot* and *photcal*. The small variations of the airmass during our observations did not allow us to estimate the atmospheric extinction coefficients from our own data. We therefore fixed the extinction coefficients at their mean values adopted from the NOT homepage: $k_B = 0''.22$ and $k_V = 0''.12$. Since the target and the standard stars had small airmass differences the uncertainties in the airmass correction has a negligible effect on our photometry. As a result of the photometric fit, we obtained the following zeropoints $B_{ZP} = 25^m.62 \pm 0.01$ and $V_{ZP} = 25^m.51 \pm 0.01$, and color terms $BV_b = 0''.036 \pm 0.011$ and $BV_v = -0''.068 \pm 0.014$.

² USNO-B1.0 stars used for the astrometric transformation of the 3C 58 field: 1548-0060227, 1548-0060191, 1548-0060258, 1548-0060348, 1548-0060300, 1548-0060306 1548-0060264, 1548-0060155, 1548-0060199, 1547-0060002, 1547-0060015.

¹ www.not.iac.es/instruments/alfosc

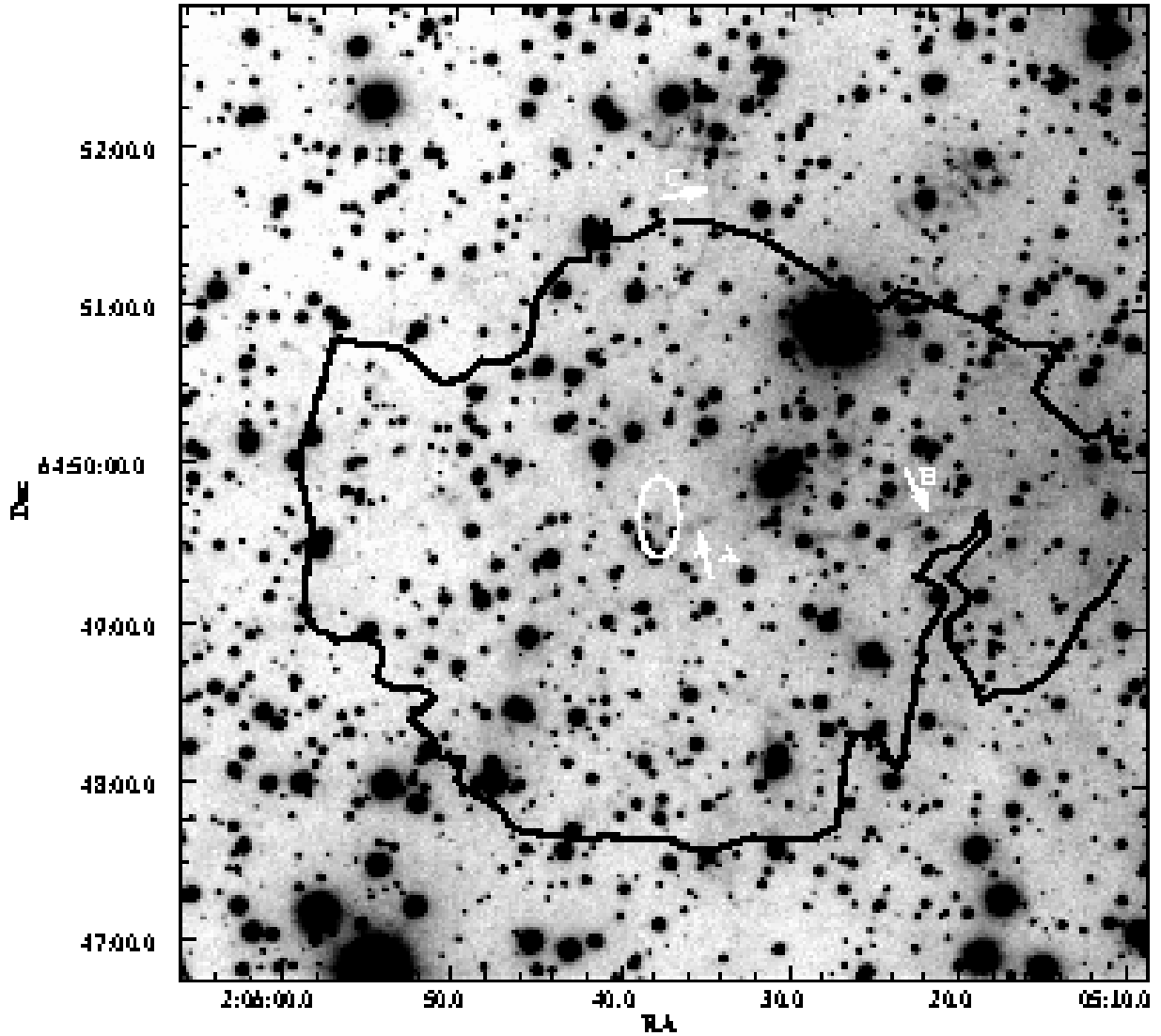


Fig. 1. Overview ($\sim 6' \times 6'$) of the center of the supernova remnant 3C 58 in the B -band, as obtained with NOT/ALFOSC. An outer contour of X-ray emission of the 3C 58 plerion is overlaid from the Chandra/ACIS-S image. A bold ellipse in the plerion center marks the position where the pulsar J0205+6449 powering the nebula is located. The central region is enlarged in Fig. 2. White arrows marked “A”, “B” and “C” point at some filaments belonging to the remnant. Filament A is discussed further in Fig. 2.

3. Results

3.1. Overview of the 3C 58 field

The NOT/ALFOSC overview of the 3C 58 field in the B band is shown in Fig. 1. The field is crowded with stars which makes it difficult to immediately identify any optical counterpart of the plerion’s X-ray emission, whose outer contour from an archival Chandra/ACIS-S image³ is overlaid. Nevertheless, one can resolve several bright optical filaments likely associated with the SNR, e.g., a long filament extending from the center of the nebula in the E-W direction. The brightness of the extended optical

emission increases toward the X-ray tail west of the plerion. The same is seen in our V image and in a red Palomar plate (van den Bergh, 1978; Fesen, 1983). The long E-W filament also correlates with this tail and it is clearly detected in narrow band $H\alpha$ and [O III] images (Fesen et al., 2008). Optical spectra of some central parts of the filament have been obtained by Fesen (1983) and reveal a radial velocity of up to 900 km s^{-1} confirming that it belongs to the SNR. Whether the other small scale optical BV filaments and knots are associated with similar structures detected in the radio, narrow band optical, and/or X-rays is outside the scope of this paper. Here we concentrate on the faint extended emission located in the center of the image near/within the region marked in Fig. 1 by a bold ellipse that contains the pulsar.

³ The X-ray data were retrieved from the Chandra archive (Obs ID 4382, 2003-04-23, 170 ks exposure, PI P. Slane).

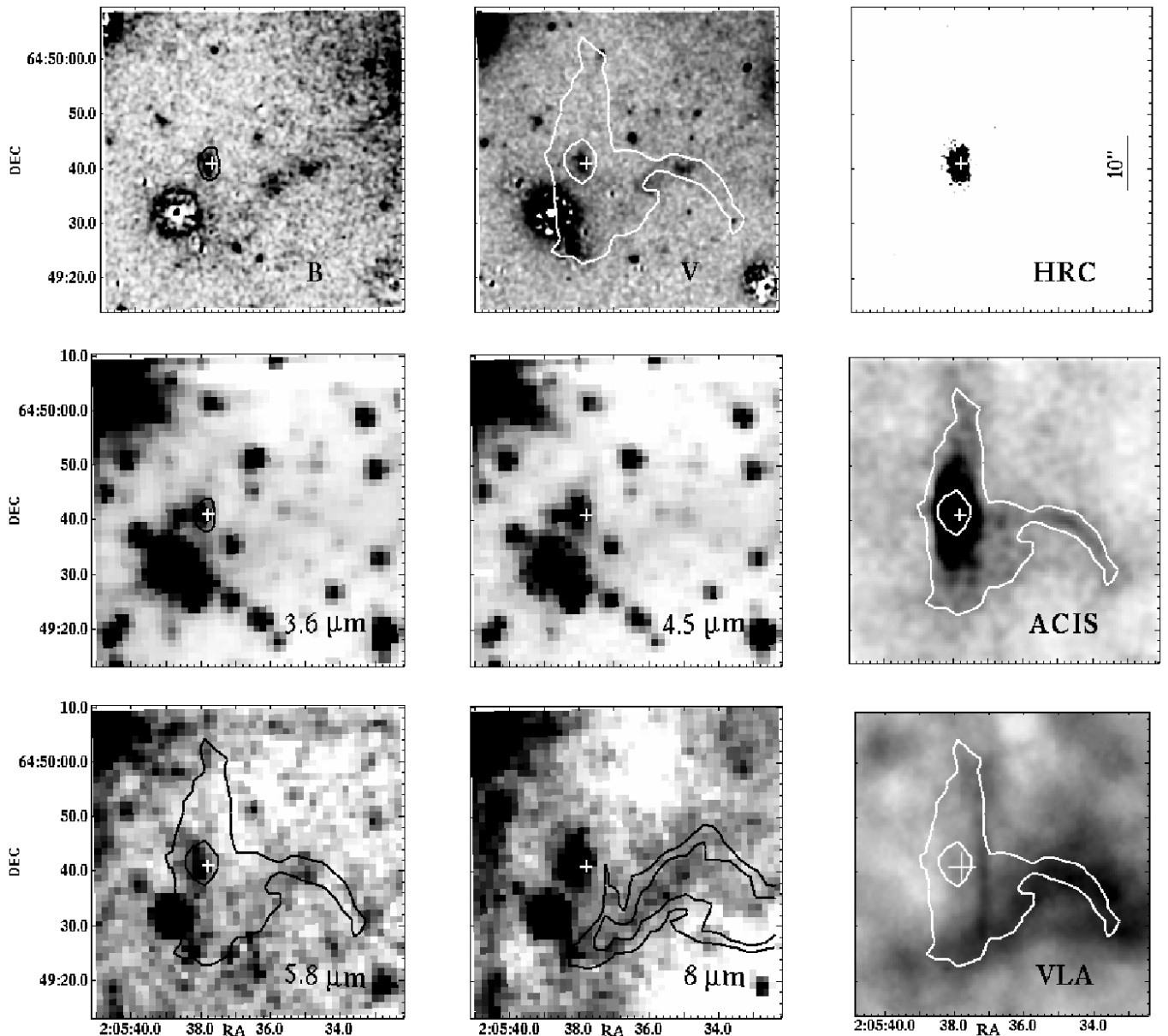


Fig. 2. Central $\sim 1'1 \times 1'1$ part of 3C 58 containing the pulsar and the PWN. *Top-Left* and *Top-Middle* panels are NOT/ALFOSC *B* and *V* band images, respectively, where unsaturated field stars have been subtracted to better reveal the suggested pulsar/PWN optical counterpart. Other panels show images of the same field but in X-rays, mid-IR and radio, as obtained with the Chandra/HRC and Chandra/ACIS, Spitzer/IRAC and VLA, respectively, as indicated in the images. The optical and X-ray images have been smoothed with a Gaussian kernel of three pixels. The X-ray contours outlining the boundary and PWN brightness distribution in X-rays on the HRC and ACIS images are overlaid on the *B*, $3.6 \mu\text{m}$ and on the *V*, $5.8 \mu\text{m}$ and VLA images, respectively. The VLA contours are shown in the $8 \mu\text{m}$ image. The white cross (“+”) in all panels marks the Chandra/HRC position of the pulsar (Murray et al., 2002). Filament “A” in Fig. 1 is clearly seen in both *B* and *V* to the west of the white cross.

3.2. Detection of the pulsar/PWN optical counterpart

The region containing the pulsar is enlarged in Fig. 2, where we compare our optical *B* and *V* images with available archival images obtained in other spectral domains: Chandra/ACIS-S and HRC-S⁴ X-ray images, mid-infrared images obtained with

Spitzer/IRAC⁵, and a 1.4 GHz VLA radio image (Bietenholz, 2007). The unsaturated stars closest to the pulsar were subtracted in the optical images. The dynamical range of the ACIS image was changed compared to the contour shown in Fig. 1 to reveal the structure of the torus-like PWN with its possible western jet (assuming the torus is seen edge-on).

In both optical bands (*Top Left and Middle* panels of Fig. 2) we detect a faint extended, elliptical structure at the pulsar po-

⁴ The X-ray data were retrieved from the Chandra archive (Obs ID 1848, 2002-01-09, 33.5 ks exposure, PI S. Murray).

⁵ Program ID 3647, exposure 5.4 ks, PI P. Slane

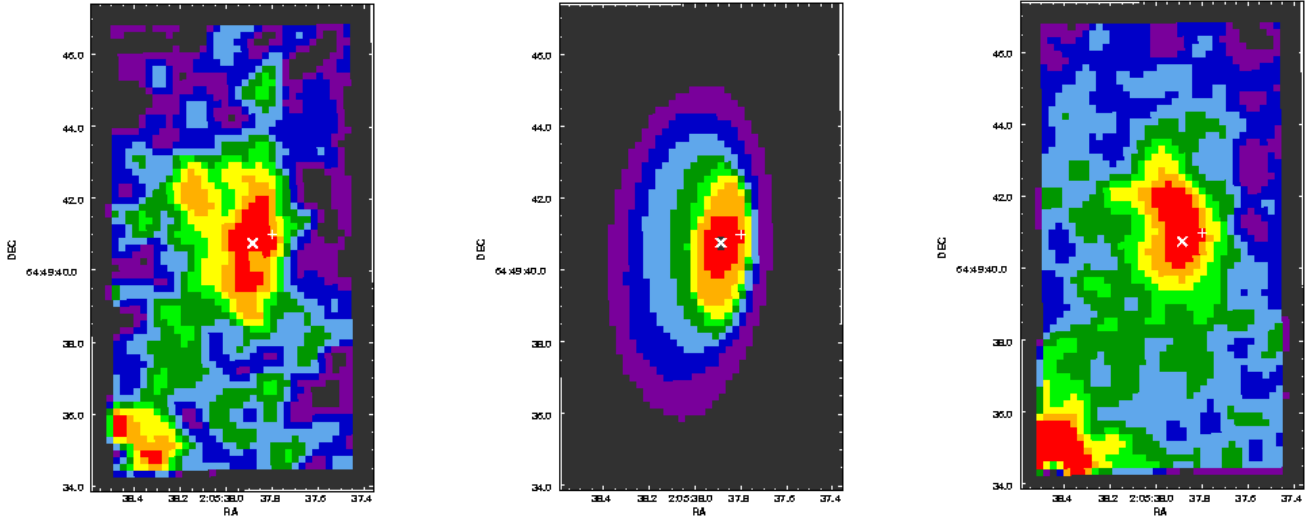


Fig. 3. The $13'' \times 6''$ central region of 3C 58 with the suggested optical counterpart of the pulsar/PWN system in the *B* (Left) and *V* (Right) bands and results of the *B* band surface brightness fit with elliptical isophotes (Middle). As in Fig. 2, the white plus sign marks the HRC-S X-ray position of the pulsar while “x” shows the position of the center of the brightest part of the optical source obtained from the fit. The difference between the plus and x is $\approx 0''.6$, which is about twice smaller than the $1-\sigma$ uncertainty of the pulsar X-ray position combined from $\sim 1''$ HRC pointing accuracy and $\sim 0''.1$ uncertainty of the astrometric referencing of the optical images. The *B* and *V* images were smoothed with a Gaussian kernel of three pixels. The bright source at the bottom left corner of the *B* and *V* images is the remains of a poorly subtracted field star.

sition and we have marked this by a white plus sign. Its morphology matches the structure seen in the HRC image, which reveals only the brightest part of the PWN in X-rays. Both the extent of this elliptical optical source and the orientation of its major axis are similar to what is found in X-rays. This suggests that the detected source is the optical counterpart of the PWN of PSR J0295+6449, with perhaps also a contribution from the pulsar itself. The source is also clearly visible in all four IRAC mid-IR bands at the same position and with the same elliptical morphology and orientation. An $8\ \mu\text{m}$ image of this field was presented by Slane (2007) and Slane et al. (2008). The astrometric accuracy of the pipeline produced mid-IR post-BCD (Basic Calibrated Data) images shown in Fig. 2 is $\sim 0''.2$, which allows us to state that structures we see in the optical and IR represent the same source. The mid-IR counterpart appears to be slightly blurred in comparison with the optical structures. This is because of the lower spatial resolution of the IRAC images (pixel size of $1''.2$) compared to that in the optical (pixel size of $0''.19$).

In the optical we also see two knots on an extended filament west of the pulsar (called Filament “A” in Fig. 1). They coincide spatially with an elongated X-ray structure seen in the ACIS image that has been interpreted as a possible jet emanating from the pulsar (Slane et al., 2002). However, in the optical images we do not see the “beginning” of the jet. The same is true for the mid-IR where we see both faint emission from the filament and the knots, in particular the western-most of the two optical knots. The filament, and especially the knots, are best seen at the longest IR wavelengths. These structures seen in the optical and mid-IR are likely parts of a long curved SNR filament clearly visible in the VLA radio image (Bottom-Right panel of Fig. 2). To emphasize this, we have overlaid the radio

contours on the $8\ \mu\text{m}$ image. The $8\ \mu\text{m}$ emission traces the radio structure well. At shorter wavelengths, and in particular in the optical, the full structure of the radio emission becomes less obvious. That the emission becomes stronger, is less clumpy, and traces the radio structure progressively better as the wavelength increases from the *B*-band to $8\ \mu\text{m}$, makes us confident that we have indeed identified the optical/IR counterpart to the radio filament. The X-ray contours overlaid on the radio image also show that at least the distant part of the elongated X-ray structure is likely of the same origin as the radio filament. This rules out the interpretation of this part of the structure as the pulsar jet.

To compare the suggested optical counterpart to the X-ray PWN torus structure, we have fitted the spatial intensity distribution with a simple two-dimensional model (using the IRAF isophotes package) accounting for the brightness distribution by elliptical isophotes and taking into account the background level. The same was done by Murray et al. (2002) for the extended part of the X-ray source in the HRC image, using CIAO Sherpa tools. The results of the spatial fits are presented in Fig. 3 and in Table 1.

The fit shows that the brightest part of the optical nebula, within $1''$ – $2''$ of the center, has almost a circular shape and emits only $\lesssim 10\%$ of the total flux. If our identification is correct, this can be considered as an upper limit of the pulsar contribution to the total pulsar+PWN optical flux. This is consistent with what was found for two known pulsar+PWN systems in the optical range (Serafimovich et al., 2004). The coordinates of the center defined from the fit are $\text{RA}=02:05:37.88$ and $\text{DEC}=64:49:40.7$ (marked by “x” in Fig. 3). This is in agreement with the pulsar X-ray coordinates (marked by plus), $\text{RA}=02:05:37.8$ and $\text{DEC}=64:49:41$ (Murray et al., 2002),

Table 1. Parameters of the elliptical fit to the surface brightness of the PSR J0295+6449+PWN optical counterpart ordered by the major ellipse axis length (c.f., *Middle panel* of Fig. 3).

Center ^a RA	Center ^a DEC	Major axis length	Ellip- ticity ^b	PA ^c N to E	B-band flux ^d
02:05:*	64:49:*	arcsec		degrees	%
37.88	40.7	0.84	0.28	-7.29	3.1(0.8)
37.88	40.7	1.26	0.28	-7.29	7.6(1.2)
37.88	40.7	1.9	0.28	-7.29	17.4(1.7)
37.88	40.7	2.86	0.56	-16.13	22.9(2.2)
37.88	40.7	4.28	0.62	-3.68	40.9(3.1)
38.00	40.8	6.42	0.48	-3.68	86.3(6.6)
38.00	40.5	9.62	0.59	-5.40	100

^a coordinates of centers of the ellipses (J2000);

^b defined as $1 - l_{\min}/l_{\max}$, where l_{\min} and l_{\max} are the minor and major ellipse axes lengths, respectively;

^c positional angle of the major axis;

^d flux from the elliptical aperture normalized to the flux from the largest aperture in this set. Numbers in brackets are 1σ uncertainties.

when accounting for our astrometrical uncertainty, $\lesssim 0''.1$, and the typical HRC pointing uncertainty, $\lesssim 1''$. The ellipticity increases up to ~ 0.5 – 0.6 for the outer optical nebula regions, and the major axis is slightly tilted towards the North-West by a few degrees, which is also in a good agreement with what was found in X-rays (Murray et al., 2002; Slane et al., 2002). In addition, the optical nebula is elongated in the north-south direction almost symmetrically around its center with a total length of $\sim 9''.6$, which agrees with the $\sim 10''$ extent of the brightest part of the nebula in the HRC-S data. Finally, assuming that we see a tilted torus-like shaped nebula, our elliptical fit suggests that the angle of the torus symmetry axis to the sky plane is in the range of 53° – 66° . This is close to the value of $\sim 70^\circ$ estimated from the X-ray data by Slane et al. (2002).

To bring out more details of the structure of the nebula in the optical/mid-IR and in X-rays, we considered also 1D-spatial profiles of the presented images along two slices shown in Fig. 4. The slices are $2''$ wide with PA 0° and 90° , both centered on the HRC-S pulsar position. The first slice is $20''$ long to include the most north-south extent of the nebula as seen in the ACIS-S image and was placed symmetrically over the center of the nebula. The second slice is $40''$ long and extends toward the west to cover also the region supposed to be an X-ray emitting jet. The X-ray, optical and mid-IR spatial profiles along these slices are presented in Fig. 5. The horizontal axis in the *Left panel* is directed from south to north, and in the *Right panel* from east to west.

This figure shows the coincidence of the positions of the main peak of the nebula in the optical, mid-IR and in X-rays. The ACIS-S peak is broader than that of the HRC because of the lower spatial resolution of ACIS. The same is true for the infrared where we show only the $8\ \mu\text{m}$ profile. The $5.8\ \mu\text{m}$ profile is practically the same, while the $3.6\ \mu\text{m}$ and $4.6\ \mu\text{m}$ profiles are contaminated by the nearby star east of the pulsar. In the *Left panel* the ACIS-S peak has an apparent offset toward north by roughly an arcsecond, but this may be related

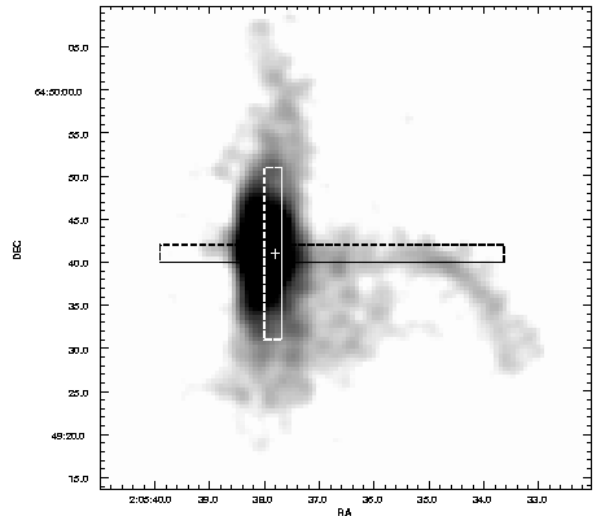


Fig. 4. ACIS-S image with positions of two slices of $40''$ (black) and $20''$ (white) lengths and of $2''$ widths used for the comparison of the X-ray and optical spatial profiles of the pulsar+PWN system in Fig. 5.

to errors in the astrometrical referencing of the ACIS-S image (Slane et al., 2002, 2004). The profiles confirm that we see the same source in all three spectral domains. Although the position of the main optical and IR peaks coincide with the pulsar X-ray position, we do not resolve any point-like object in the center of the nebula in our optical and the archival IR images. The FWHM of the optical PSF is $\sim 0''.7$ – $0''.85$ (Sect. 2.1), while for the mid-infrared it varies with the wavelength from $\sim 2''.1$ to $2''.5$. The brightest part of the PWN, which subtends several arcseconds, is clearly resolved (Fig. 5). To resolve the point-like pulsar from the nebula in the optical/IR would require deeper imaging at high spatial resolution, or alternatively time resolved observations.

We also note a broad secondary peak west of the pulsar seen in the east-west optical and IR profiles and which is marked by a vertical dotted line in the *Right panel* plot of Fig. 5. It coincides with a shallow secondary peak seen in the ACIS profile. This is Filament “A” in Fig. 1 with its knots, and which is projected on the extended X-ray structure which was early supposed to be the pulsar jet.

To summarize this part, we conclude that the coincidence of the center positions of the detected optical/mid-IR nebula with that of the pulsar/PWN X-ray source, the optical/mid-IR/X-ray morphology and the spatial surface brightness profiles in these wavelength regions, strongly support that we have indeed detected the optical/mid-IR counterpart of the pulsar/PWN system in the 3C 58 supernova remnant.

3.3. Optical and mid-IR photometry

Optical photometry of the suggested counterpart was performed on the star subtracted images. We used the elliptical apertures from the surface brightness fit described in Sect. 3.2. The parameters of the ellipses are presented in Table 1. The backgrounds were estimated from a circular annulus with a ~ 20

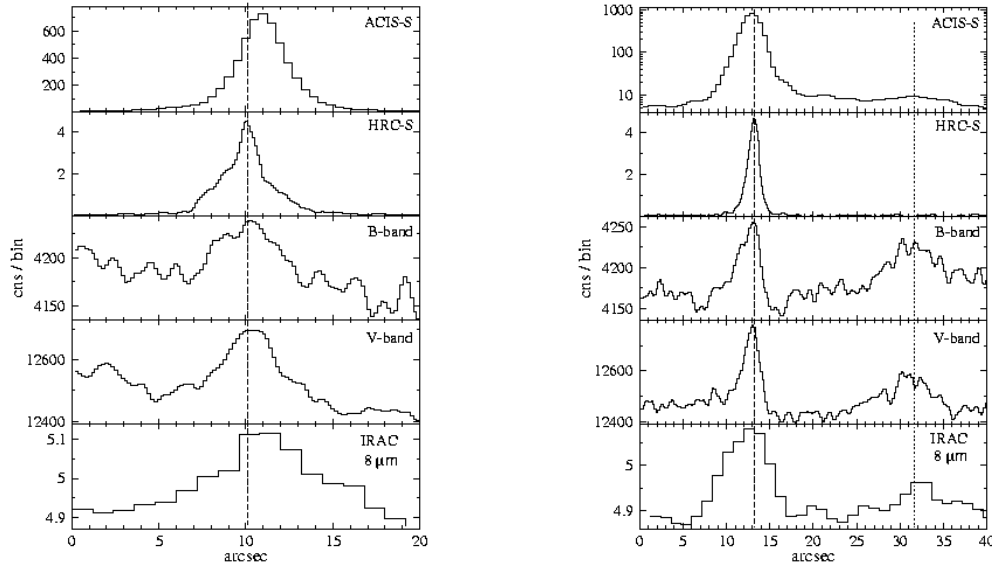


Fig. 5. Spatial profiles of the pulsar/PWN system in the optical, mid-infrared and X-rays along the north-south (*Left*) and east-west (*Right*) slices shown in Fig. 4 obtained from different images, as indicated in the plot. The coordinate origins of the horizontal axes correspond to Dec=64:49:31:00 and RA=02:05:39:90 for the *Left* and *Right* plots, respectively. The images were smoothed with a 3-pixel Gaussian kernel. Dashed vertical lines indicate the HRC-S position of the pulsar. Dotted line shows the position of a bright jet-like structure to the west, before it bends to the south. The ACIS-S profile in the right panel is in a log scale to better resolve this structure in X-rays.

pixel inner radius and a width of ~ 10 pixels centered on the nebula center. The relative photometric errors were minimized ($S/N \approx 13$) for the aperture that formally encapsulates $\geq 86\%$ of the total elliptic nebula flux. The measured magnitudes of the integral pulsar/torus nebula emission are $B = 24^m06 \pm 0.08$ and $V = 23^m11 \pm 0.04$. We also tried circular and polygonal apertures of different geometries to better encapsulate the whole flux, but got practically the same results. The magnitudes were transformed into fluxes using the zero-points provided by Fukugita et al. (1995). The results are summarized in Table 2. The magnitude distribution with the nebular radius can be estimated using these magnitudes and the normalized fluxes for all elliptical apertures which are given in Table 1.

All nearby background stars were also successfully subtracted from the Spitzer/IRAC pipeline post-BCD mid-IR images using the *psf* and *allstar* IRAF utils. Then aperture photometry with circular apertures was done using *daophot* tasks in accordance with prescriptions given in the IRAC Observers Manual⁶. A typical aperture radius, where the curves of growth saturate, was about 6–7 pix, or $7''.2$ – $8''.4$ depending on the band, and the annulus for backgrounds was 8–12 pixels. An example of the aperture choice for the $5.8 \mu\text{m}$ image is shown in Fig. 6. We repeated the star subtraction procedure and varied the background region. The differences in the magnitudes obtained were about the measurement statistical errors and they were included in the resulting uncertainties. The magnitudes were converted into fluxes in physical units and the results are presented in Table 2. Extended source aperture corrections

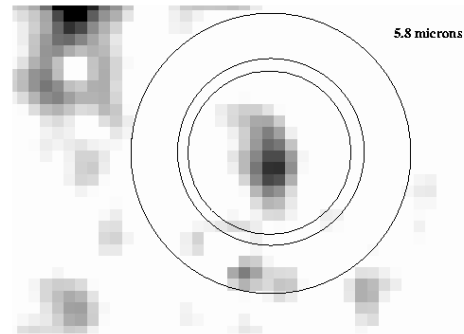


Fig. 6. Enlarged image of the pulsar/PWN candidate counterpart at $5.8 \mu\text{m}$. Nearby background stars have been subtracted and the image was smoothed with a $2''.4$ Gaussian kernel. Circles with $8''.4$, $9''.6$, and $14''.4$ radii show the aperture and background annuli used for the photometry.

were applied for the flux values⁷ and the flux errors are combined from the magnitude measurement errors and $\sim 5\%$ IRAC calibration uncertainties in each band.

As seen from Table 2 the measured mid-IR fluxes have larger uncertainties than the optical ones. The main reason is the faintness of the mid-IR source which is detected at about the 5σ level. The 10%–15% uncertainties introduced by using the pipeline produced mosaic IR-images does not exceed the count statistic errors and cannot considerably change the results. Thus, we confirm, but at a higher level of significance, the 2σ mid-IR detection reported by Slane et al. (2008). The

⁶ see, e.g., ssc.spitzer.caltech.edu/archanaly/quickphot.html

⁷ ssc.spitzer.caltech.edu/irac/calib/extcal/index.html

Table 2. Observed magnitudes and fluxes for the presumed optical/infrared pulsar/PWN counterpart of 3C 58, as well as dereddened fluxes for different values of A_V .

λ_{eff} (band)	Mag. obs. ^a	log Flux obs. ^a	log Flux dred. ^a		
			$A_V=1.9$	2.9	3.4
(μm)	(mag)	(μJ)	(μJ)	(μJ)	(μJ)
440(B)	24.06(8)	-0.02(3)	0.99(3)	1.52(3)	1.78(3)
530(V)	23.11(4)	0.31(2)	1.10(2)	1.52(2)	1.73(2)
650(R) ^b	>22.5(5)	0.48(20)	1.11(20)	1.44(20)	1.61(20)
3.6	15.8(4)	2.14(16)	2.19(16)	2.22(16)	2.23(16)
4.5	15.2(4)	2.16(14)	2.20(14)	2.22(14)	2.22(14)
5.8	14.3(3)	2.34(11)	2.38(11)	2.40(11)	2.41(11)
8.0	13.5(2)	2.42(9)	2.46(9)	2.48(9)	2.49(9)

^a numbers in brackets are 1σ uncertainties referring to last significant digits quoted

^b upper limit for the pulsar magnitude taken from Fesen et al. (2008)

difference between the mid-IR and the optical fluxes is quite significant, and allows us to draw conclusions on the multi-wavelength spectral energy distribution (SED) of the suggested counterpart.

3.4. Multiwavelength spectrum of the pulsar+PWN source

We can use our fluxes estimated for the pulsar/PWN counterpart candidate together with the X-ray data to construct a tentative multiwavelength spectrum for the central part of the nebula. When compiling data from the IR to X-rays one has to take into account that the PWN torus size in the optical and IR appears smaller than in the X-rays. Future deeper optical and IR studies will probably reveal fainter outer parts of the torus in these ranges, as has been seen for the Crab and PSR B0540-69 PWNs. These fainter but more extended outer parts can contribute considerably to the total flux of the system.

At the current stage it is reasonable to compare the measured optical and infrared fluxes with the X-ray spectrum extracted from the same physical region. To do that we extracted the X-ray spectrum for the central part of the torus region from the ACIS-S data making use of the CIAO *acispec* tool and the same elliptic aperture we applied for the optical source photometry. This gave ~ 30200 source counts. The spectral data were grouped to provide a minimum of 20 counts per spectral bin and fitted by an absorbed power-law model using standard XSPEC tools. We obtained a statistically acceptable fit with the photon spectral index $\Gamma = 1.88 \pm 0.08$, the absorbing column density $N_H = (4.34 \pm 0.08) \times 10^{21} \text{ cm}^{-2}$, and a normalization constant $C = (4.39 \pm 0.17) \times 10^{-4} \text{ photons cm}^{-2} \text{ s}^{-1} \text{ keV}^{-1}$. The fit had $\chi^2 = 0.95$ per degree of freedom. Within the uncertainties the Γ and N_H values obtained are in agreement with those obtained for the entire torus by Slane et al. (2004), while the unabsorbed integral flux, $1.68 \times 10^{-12} \text{ erg cm}^{-2} \text{ s}^{-1}$ (0.5–10 keV range), is only $\sim 40\%$ of that from the entire X-ray torus region. The derived unabsorbed X-ray spectra for both the inner region and the entire torus regions are shown in Fig. 7.

Before comparing with the X-ray spectrum we need to correct the optical and IR data for interstellar reddening. The interstellar color excess towards 3C 58 is, however, not well constrained. Fesen (1983) estimated, based on the $H\alpha/H\beta$ decrement obtained from spectral observations of a part of the bright long E-W filament discussed in Sect. 3.1, that $E(B-V) = 0.6 \pm 0.3$ mag, assuming an intrinsic $H\alpha/H\beta$ ratio of 3.0. This corresponds to the V-band reddening correction of $A_V \approx 1.9 \pm 1.0$, adopting the standard ratio $A_V/E(B-V) = 3.1$. Later spectroscopy of a sample of the remnant emission knots provided a more stringent constraint, $E(B-V) = 0.68 \pm 0.08$ mag (Fesen et al., 1988). Recent spectroscopy of three brightest $H\alpha$ -filaments in the northern part of the SNR yielded a similar result, $E(B-V) = 0.6 \pm 0.1$ mag (Fesen et al., 2008).

We also know that 3C 58 sits within the Galactic disk ($l \approx 130^\circ.4$, $b \approx 3^\circ.04$) and that the entire Galactic excess in this direction provided by Schlegel et al. (1998) is $E(B-V) \approx 0.99$ mag. This is consistent with the fact that the Galactic disc edge in this direction of the sky is roughly 1–2 kpc more distant from us than 3C 58. Assuming a linear color excess increase with the distance from the Sun with a mean gradient of $\sim 0.2 \text{ mag kpc}^{-1}$ applicable within 3–4 kpc of the solar neighbourhood (e.g., Bohlin et al., 1978), we obtain $E(B-V) \sim 0.6$ for 3C 58 and ~ 1 mag as the entire excess, respectively, provided that the distances to 3C 58 and the disc edge are 3.2 kpc and ~ 5 kpc. This is in good agreement with the estimates above.

On the other hand, using $N_H = (4.34 \pm 0.08) \times 10^{21} \text{ cm}^{-2}$, derived from the above X-ray spectral fit, and the empirical relation $N_H/E(B-V) = 4.8 \times 10^{21} \text{ cm}^{-2} \text{ mag}^{-1}$ applicable for the Milky Way (Bohlin et al., 1978), we obtain $E(B-V) = 0.9 \pm 0.02$ mag ($A_V = 2.8 \pm 0.06$). Another empirical relation between the effective N_H of the X-ray absorbing gas and the dust extinction, $N_H/E(B-V) = (5.55 \pm 0.093) \times 10^{21} \text{ cm}^{-2} \text{ mag}^{-1}$ (Predehl & Schmitt, 1995), gives a smaller value, $E(B-V) = 0.78 \pm 0.03$ mag. The color excesses based on the N_H value, derived from the X-ray spectral fit of the torus emission, are systematically higher than the mean excess obtained from the optical studies. This may be explained by intrinsic reddening variations over the remnant area resulted from a nonuniform distribution of the SN ejecta.

Summarizing all the uncertainties of the color excess we select for our further analysis $A_V = 1.9$ mag as a most plausible reddening consistent with the mean excess given by the optical studies. We also perform the analysis for $A_V = 2.9$ which is compatible with the X-ray spectral estimates discussed above. Dereddened optical/IR fluxes are presented in Table 2. For dereddening we used a standard optical extinction curve (Cardelli et al., 1989) and average A_λ/A_K ratios provided especially for the Spitzer/IRAC bands by Indebetouw et al. (2005).

We have combined dereddened optical/IR fluxes for the pulsar/PWN system with the unabsorbed X-ray spectrum in Fig. 7. As expected, the shape of the multiwavelength spectrum strongly depends on A_V . To emphasize this we have also included an even higher value for the extinction towards 3C 58, with $A_V=3.4$ mag. This value corresponds to the upper limit of Galactic extinction in the given direction as de-

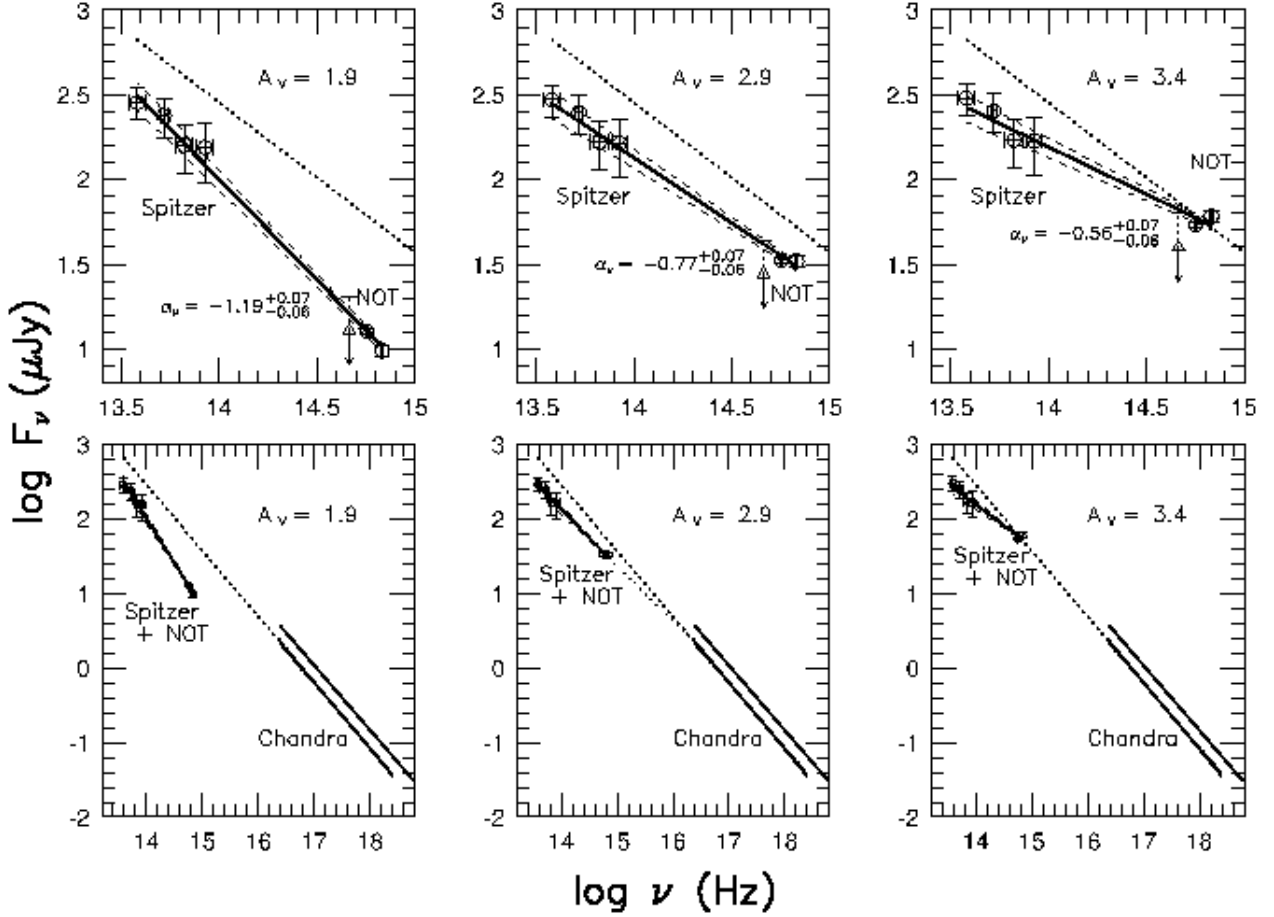


Fig. 7. Tentative unabsorbed multiwavelength spectrum for the inner part of the torus region of the 3C 58 pulsar/PWN system compiled from data obtained with different telescopes, as indicated in the plots. Different panels demonstrate the dependence of the spectrum on the adopted interstellar extinction A_V . The *Lower and Upper panels* show the whole IR/X-ray spectral range and its enlarged optical/IR part, respectively. Both the optical/IR and X-ray data are fitted with power laws with different spectral indices (defined as $F_\nu \propto \nu^{\alpha_\nu}$). The derived indices for the optical/IR part are shown in the *Upper panels* and dashed lines constrain 1σ uncertainties of the respective fits. For the X-ray part, the lower power law is for the inner part of the torus (i.e., same as for the optical/IR emission), whereas the upper power law is for the entire torus. The power-law indices for these X-ray data are -0.88 ± 0.08 and -0.87 ± 0.02 , respectively. Dotted lines show extensions from the optical/IR part and the X-ray part. Grey polygons (barely resolved) are 1σ uncertainties of the X-ray fits. For the optical/IR range the steepness of an assumed power law depends strongly on A_V , with an upper limit of $\alpha_\nu \sim -0.5$. For $2.9 \leq A_V \leq 3.4$, the optical/infrared spectrum can be joined with the X-ray spectrum using only one spectral break. Lower extinctions suggest a more complicated multiwavelength spectrum. The upper limit for the pulsar flux in the R band (Fesen et al., 2008) is included. Its possible uncertainty (0.5 mag) is marked by a dashed errorbar. See text for further details.

rived from the total neutral hydrogen Galactic column density, $N_H = 5.34 \times 10^{21} \text{ cm}^{-2}$ (Kalberla et al., 2005), making use of the relation by Bohlin et al. (1978). This higher value of extinction is included because it represents an interesting limiting case for the dereddened spectral energy distribution (see below). In Fig. 7 we have plotted the power-law describing the X-ray spectrum from the entire PWN torus (upper X-ray power law). We also show the X-ray spectrum from the only same physical region as for the optical/IR emission (lower X-ray power law).

In all cases the optical/IR SED can be fitted by a power law ($F_\nu \propto \nu^{\alpha_\nu}$) and the spectral indices, α_ν , of the fits are shown in the upper panels of Fig. 7. For the most plausible A_V value

of 1.9 the fit residuals are minimal and we see a monotonous decline in flux from the IR to the optical, suggesting a non-thermal nature of the detected optical/IR counterpart candidate. This implies a synchrotron emission mechanism for the detected nebula, normally considered to be the main radiative process for PWNe. For higher extinction values, particularly for $A_V = 3.4$, the spectrum becomes flatter.

The upper limit of the pulsar point source flux in the R -band obtained by Fesen et al. (2008) is also shown in the plots for comparison. It was not included in the fits and we estimate that its uncertainty can be as large as half a stellar magnitude. This is because it was derived from a comparison with rather uncertain catalogue magnitudes of USNO stars in the 3C 58

field. We included the possible flux uncertainty in Table 2 and Fig. 7. The pulsar R -band flux upper limit is a factor of a few lower than the expected nebula flux in this band, which is compatible with our estimates for the pulsar flux contributions in the B and V bands (see Sect. 3.2).

Extending the X-ray spectral fits (*dotted lines*) toward the optical/IR bands, and *vice versa*, we see that at any adopted A_V the X-ray extension overshoots the IR fluxes. For the A_V range of ~ 2.9 – 3.4 the multiwavelength spectrum from the IR through X-rays can be modeled by a power law with a single break and a flatter slope in the IR/optical range. In the optical/IR range the spectrum cannot be shallower than that with $\alpha_V \sim -0.5$, as follows from the largest value of $A_V = 3.4$ (*Right panels*), when the break occurs directly in the B optical band. For lower A_V the break moves toward the X-ray range and at $A_V = 2.9$, it meets the low-energy boundary of the X-ray range (*Middle panels*). In this case the optical/IR slope with $\alpha_V \approx -0.8$ is close to that in X-rays with $\alpha_V \approx -0.9$. For lower values of A_V the intrinsic optical/IR spectrum becomes steeper and we must invoke more breaks to connect the optical/IR SED with the X-ray spectrum. For example, at $A_V = 1.9$, the optical/IR spectral index, $\alpha_V \approx -1.2$, is significantly lower than that in X-rays (*Left panels*).

The Crab and PSR B0540-69 are the only two PWNe previously detected in the optical and mid-IR ranges. Even within the large uncertainties of the interstellar extinction toward 3C 58, the tentative multiwavelength spectrum of the 3C 58 PWN can be similar to either the Crab PWN (for $A_V \gtrsim 2.9$), or the PWN of PSR B0540-69 (for $A_V \lesssim 2.9$). The Crab PWN changes smoothly its spectral slope from negative in X-rays with $\alpha_V \sim -1$ to a flatter value in the optical, whereas the spectrum of the PSR B0540-69 PWN demonstrates a double-knee structure at the transition from the optical to X-rays (e.g., Serafimovich et al., 2004). Our preferred value of $A_V \sim 1.9$ suggests that the 3C 58 PWN is likely similar to the latter case.

We emphasize the importance of using the same spatial region in all spectral domains when constructing the multiwavelength spectrum. As seen from the *Bottom panels* of Fig. 7, using the entire torus X-ray spectrum, instead of its inner region, would lead to different conclusions. To make a meaningful multiwavelength plot for the entire X-ray emitting PWN torus, we would need deeper optical/IR observations to constrain the emission in the outer parts of the torus, and to make a more detailed comparison with the entire PWNe of the Crab and PSR B0540-69 and with available theoretical models.

4. Discussion

The properties of the detected source indeed suggest it to be the optical/mid-IR counterpart of the 3C 58 pulsar/PWN torus system. The alternative could be a SNR filament, or possibly a faint background spiral galaxy seen edge on and coinciding by chance with the pulsar position. However, the positional coincidence with the X-ray PWN torus and the remarkable similarity of the object morphology and orientation with those in X-rays is reassuring. The multiwavelength spectrum shows that the optical and mid-infrared magnitudes of the proposed counterpart are at least consistent with the spectra seen in other PWNe. We

argue that this makes the alternative interpretations rather unlikely.

There are no significant radio filaments at the PWN position (Bietenholz, 2007). The nearest bright and sharp long filament known as a “wisp” (Frail & Moffett, 1993) is a few arcseconds west of the PWN torus and the optical/IR source boundaries. Some signs of a faint radio counterpart of the PWN torus and/or the optical source may be present in the latest VLA 1.4 GHz image published by Bietenholz (2007, Fig. 2).

For an A_V value consistent with the N_H column density derived from the X-ray spectral fit there are $\sim 1\sigma$ deviations of the B and V fluxes from the best power law fit line describing the optical and mid-IR SED of the suggested counterpart (see *Middle panels* of Fig. 7). Additional optical observations are in progress to extend the SED toward the red and UV optical bands and to see if these deviations are significant and if they can better constrain the extinction value, assuming a single power-law fit of the optical/IR SED. Higher spatial and/or timing resolution are necessary to measure reliably the optical emission from the point-like pulsar embedded in the center of the PWN torus and to confirm finally the suggested identification. Longer wavelength mid-infrared imaging with the Spitzer/MIPS is needed to see if there is a break toward the radio to support the apparent absence/presence of the putative PWN torus counterpart in the radio range.

At larger spatial scales the spectrum from the whole 3C 58 plerion region from radio through X-rays is described by a power law with a single low frequency break near ~ 50 GHz. Below this frequency the spectral slope is significantly flatter than in X-rays (cf. Slane et al., 2008). This is in contrast to the plerion core near the pulsar. For the PWN torus our optical data suggest at least one break at much shorter wavelengths, somewhere between the optical and X-ray ranges. This implies a different spectrum of the relativistic particles in the plerion core at distances from the pulsar comparable to the pulsar wind termination shock radius where the PWN torus structure is formed. At any reasonable assumption on the interstellar extinction value, the optical/IR part of the power-law torus spectrum cannot be flatter than that with $\alpha_V = -0.5$ and steeper than that with $\alpha_V = -1.2$. Comparison with the radio flux from the torus or its upper limit would provide additional constraints of the spectrum of the emitting particles.

Assuming that we have indeed detected the optical/IR counterpart of the torus-shaped PWN, we compare in Table 3 its parameters with the parameters of the other two young pulsar/PWN systems which have been detected in the optical, infrared and X-rays. We also include the older Vela pulsar whose PWN has not yet been identified in the optical or IR (e.g., Shibano et al., 2003). For 3C 58 we adopt a distance of 3.2 kpc (Slane et al., 2004). Its optical luminosity uncertainty is mainly due to the uncertainty in the interstellar extinction. The ratio of the pulsar to PWN optical luminosity reflects the possible contribution of the pulsar to the total pulsar/PWN optical emission, as was estimated in Sect. 3.2. The principal ranking in Table 3 is the characteristic age and/or spindown luminosity \dot{E} . The age of 3C 58 and its association with the historical supernova event of 1181 A.D. is still debated (e.g., Slane et al., 2004). We have used the characteristic age of the pul-

Table 3. Comparison of the optical and X-ray spectral indices (α_v^O, α_v^X) luminosities (L^O, L^X), efficiencies (η^O, η^X) of the three young PWNe detected in the optical/IR and X-rays. Information on the Vela PWN, not yet detected in the optical, as well as on the pulsar characteristic ages (τ), spindown pulsar luminosities (\dot{E}), PWN sizes, and the ratios of the pulsar to PWN luminosity in the optical and X-rays are also included.

PWN	τ kyr	\dot{E} $10^{37} \text{ erg s}^{-1}$	size pc	$-\alpha_v^O$	$L^{O,a}$ $10^{33} \text{ erg s}^{-1}$	η^O 10^{-5}	$-\alpha_v^X$	$L^{X,b}$ $10^{36} \text{ erg s}^{-1}$	η^X 10^{-3}	$L_{\text{psr}}^O/L_{\text{pwn}}^O$	$L_{\text{psr}}^X/L_{\text{pwn}}^X$
Crab ^c	1.24	46	1.5	0.92	4240	920	1.14	21.8	47.5	0.0017	0.046
0540 ^c	1.66	50.2	0.6-0.9	1.5	366	245	1.04	12	79.7	0.03	0.26
3C 58 ^d	5.38	2.6	0.08-0.19	0.7-1.2	0.08-0.21	0.3-0.75	0.88	5×10^{-3}	0.19	≤ 0.1	0.23
Vela ^c	11	0.069	0.14	–	–	–	0.5	6.8×10^{-4}	9.8×10^{-2}	–	0.34

^a For the optical range 1.57–3.68 eV.

^b For the X-ray range 0.6–10 keV.

^c Data are taken from Serafimovich et al. (2004).

^d This paper. The distance is assumed to be 3.2 kpc.

sar defined in the standard way as $\tau = P/2\dot{P}$ (Murray et al., 2002). We see that the 3C 58 PWN nicely fits its position in Table 3 in terms of other physical parameters. Its size, X-ray luminosity and efficiency of transformation of the pulsar rotational loss to PWN emission, $\eta^X = L^X/\dot{E}$, and the ratio of pulsar to PWN X-ray luminosity trace the general evolution tendency where the “strength” of a PWN correlates with the spindown luminosity and fades with pulsar age. Interestingly, the luminosity of 3C 58 has faded an order of a magnitude more in the optical than in X-rays, if we take the Crab PWN as a reference. For PSR 0540-69 and 3C 58 both luminosities have decreased by approximately the same factor. This perhaps means that the old estimates of the Crab PWN optical continuum luminosity based on low spatial resolution observations Veron-Cetty & Woltjer (1993) need a revision using recently available high resolution observations of this PWN. There is no strong difference for the efficiency of the 3C 58 PWN in the optical and X-rays. The same situation applies to the younger PSR 0540-69 PWN, although 3C 58 is much less efficient, as expected from its age. For the Crab, the difference is exceptionally strong, probably for the same reasons we have mentioned above. Thus, the properties of the likely optical/IR counterpart of the 3C 58 PWN suggest that the real age of the associated SNR is close to the pulsar characteristic age, but not to the historical event of 1181 A.D, as has been discussed from other points of view by Chevalier (2004) and Bietenholz (2007).

The long extended structure seen in X-rays west of the 3C 58 pulsar has been suggested to be the jet part of its PWN (Slane et al., 2004). A similar axisymmetrical jet structure of the Crab PWN has a clear optical counterpart (e.g. Hester et al., 2002). Some hints of a less pronounced X-ray jet of the PSR 0540-69 PWN are also seen in the optical (Serafimovich et al., 2004). For 3C 58 we also see a bright optical filament projected on the X-ray jet where it bends southward. However, a comparison of the optical, infrared and radio images suggests that this is not an optical jet counterpart. It may also be that this distant part of the X-ray structure does not relate to the PWN jet at all. Instead, it is most likely a long curved SNR filament, which is also clearly seen in VLA images (Bietenholz, 2007). Its position is marked in the 8 μm images of Fig. 2. Most likely,

the part of the filament we have detected in our images, is the same as was studied spectroscopically by Fesen (1983) (position 1 in his notation) using a 4'' circle aperture. Based on H α , he estimated a radial velocity of $\sim 900 \text{ km s}^{-1}$, which is similar to the overall expansion of the remnant, and to motions in the Crab. Detailed imaging and spectral studies are necessary to confirm this and to study if this extended structure is a part of the real PWN jet or not. Deeper spectral observations will also set more stringent constraints on the interstellar extinction, which is the main source of uncertainty of the estimated intrinsic optical flux of the PWN.

In conclusion, our observations have, with high probability, increased the number of the optically identified Crab-like PWNe from two to three, which should help to constrain models of these unique objects and to understand their nature.

Acknowledgements. The work was partially supported by RFBR (grants 05-02-16245, 05-02-22003), the Swedish Research Council and Nsh 9879.2006.2. The Dark Cosmology Centre is funded by the Danish National Research Foundation. The project started while PL was still a Research Fellow at the Royal Swedish Academy, supported by a grant from the Wallenberg Foundation. The data presented here have been taken using ALFOSC, which is owned by the Instituto de Astrofísica de Andalucía (IAA) and operated at the Nordic Optical Telescope.

References

- Becker, R., Helfand, D., & Szymkowiek, A., 1982, ApJ, 255, 537
- Bietenholz, M., Kassim, N., Weiler, K. 2001, ApJ, 360, 772
- Bietenholz, M., 2007, ApJ,
- Bohlin R.C., Savage B.D., Drake, J.F. 1978, ApJ, 224, 132
- Camilo, F., Stairs, I.H., Lorimer, D.R., et al. 2002, ApJ, 571, L41
- Cardelli, J. A., Clayton, G. C., Mathis, J. S. 1989, ApJ, 345, 245
- Chevalier, R. 2004, ApJ, 619, 839
- Fesen, R. 1983, ApJ, 270, L53
- Fesen, R., Kirshner, R., & Becker, R., 1988, IAU Colloq. 101: Supernova Remnants and the Interstellar Medium, 55

- Fesen, R., Rudie, G., Hurford, A., & Soto, A. 2008, *ApJS*, 174, 379
- Frail, D. A. & Moffett, D. A. 1993, *ApJ*, 408, 637
- Fukugita, M., Shimasaku, K., Ichikawa, T. 1995, *PASP*, 107, 945
- Hester, J.J., Mori, K., Barrows, D., et al. 2002, *ApJ*, 577, L49
- Indebetouw, R., Mathis, J.J., Babler, B.L. et al. 2005, *ApJ*, 619, 931
- Kalberla, P.M.W., Burton, W.B., Hartmann, D., et al. 2005, *A&A*, 440, 775
- Landolt, A. U. 1992, *AJ*, 104, 340
- Malofeev, V., Malov, O., Glushak, A. 2001, *IAU Circ.*, 7775, 2.
Edited by Green, D. W. E.
- Malofeev, V. M.; Malov, I. F.; Malov, O. I.; Glushak, A. P. 2003, *ARep*, 47, 413
- Monet, D., Levine, S., Canzian, B., et al. 2002, *BAAS*, 34, 1104
(astro-ph/0210694)
- Murray, S., Slane, P.O., Seward, F.D., et al. 2002, *ApJ*, 568, 226
- Predehl, P. & Schmitt, J.H.M.M. 1995, *A&A*, 293, 889
- Schlegel, D. J., Finkbeiner, D. P., Davis, M. 1998, *ApJ*, 500, 525
- Serafimovich, N., Shibarov, Yu.A., Lundqvist, P., Sollerman, J. 2004, *A&A*, 425, 1041
- Shibarov, Yu.A., Koptsevich, A.B., Sollerman, J., Lundqvist, P. 2003, *A&A*, 406, 645
- Slane, P., Helfand D.J., & Murray, S.S. 2002, *ApJ*, 571, L45
- Slane, P., Helfand D.J., van der Swaluw, E. & Murray, S.S. 2004, *ApJ*, 616, 403
- Slane, P. 2007, conference proceedings, "Astrophysics of Compact Objects," 2007, Huangshan, China (astro-ph:0711.1002)
- Slane, P., Helfand, D. J., Reynolds, S.P., et al. 2008, *ApJ*, (accepted, astro-ph 0802.0206v1)
- Sollerman, J. 2003, *A&A*, 406, 639
- Stephenson, F., & Green, D. 2002, *Historical Supernovae and their Remnants* (Oxford, Clarendon)
- van den Bergh, S. 1978, *ApJ*, 220, L9
- Veron-Cetty, M. P., & Woltjer, P. 1993, *ApJ*, 270, 370
- Weiler, K. & Seielstad, G. 1971, *ApJ*, 163, 455